

Weierstraß–Institut für Angewandte Analysis und Stochastik

im Forschungsverbund Berlin e.V.

Preprint

ISSN 0946 – 8633

Radiation- and convection-driven transient heat transfer during sublimation growth of silicon carbide single crystals

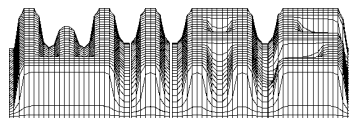
O. Klein, P. Philip, J. Sprekels, K. Wilmański

submitted: February 15, 2000

Weierstraß–Institut für Angewandte Analysis und Stochastik, Mohrenstraße 39, 10117 Berlin, Germany

Preprint No. 552

Berlin 2000



1991 Mathematics Subject Classification. 35K55, 65C20, 65M99, 80A15, 80A20.

Key words and phrases. Modeling, sublimation growth, SiC single crystal, heat transfer, radiation, convection, numerical simulation, partial differential equations.

1998 PACS numbers. 44.25.+f, 44.30.+v, 44.40.+a, 81.10.Bk, 83.10.Ff.

Edited by
Weierstraß-Institut für Angewandte Analysis und Stochastik (WIAS)
Mohrenstraße 39
D — 10117 Berlin
Germany

Fax: + 49 30 2044975
E-Mail (X.400): c=de;a=d400-gw;p=WIAS-BERLIN;s=preprint
E-Mail (Internet): preprint@wias-berlin.de
World Wide Web: <http://www.wias-berlin.de/>

Abstract

This article presents transient numerical simulations of heat transfer occurring during sublimation growth of SiC single crystals via the Modified Lely Method, investigating the respective influence of radiative and convective contributions. We give a concise treatment of the radiation model including semi-transparency via the energy-band approach and we briefly describe the corresponding numerical methods. A complete documentation of the used material data is included.

1 Introduction

Owing to numerous technical applications in electronic and optoelectronic devices, such as lasers, semiconductors and sensors, the industrial demand for high quality SiC bulk single crystals remains large. Hence, many experimental and theoretical publications of recent years have treated SiC single crystal growth with the goal of improving quality and size of the grown crystals while trying to increase the growth rate at the same time, confer e.g. [BKP+99], [BMH+93], [HHW+95], [Kan93], [Kon95], [Lil93], [Nis95], [PBD+96].

Sublimation growth via the *Modified Lely Method* has been one of the most successful and most widely used growth techniques of recent years. A graphite crucible is intensely heated by induction heating to temperatures of some 3000 K. The crucible contains a reactor, where polycrystalline SiC source powder is evaporated, resulting in a gas mixture consisting of molecules made up of silicon and carbon, Si, Si₂C and SiC₂ being the predominant species. At the same time argon is pumped into the system as inert gas. An SiC single crystal is growing via sublimation from a cooled seed.

The objective of this article is to monitor the influence of radiation and convection with respect to the heat transfer occurring during sublimation growth via the Modified Lely Method. Due to the high temperatures occurring inside the reactor, and owing to the potentially strong inert gas flow, heat transport via radiation and convection plays an important role. To study their respective influence in detail will lead to a better understanding of the physical processes inside the reactor and will provide some insight on how to control the growth conditions.

Our work is based on the transient model that has been presented in [BKP+99]. For the gas phase the model is founded on continuous mixture theory, providing balance equations for mass, momentum and energy including reaction-diffusion equations (cf.

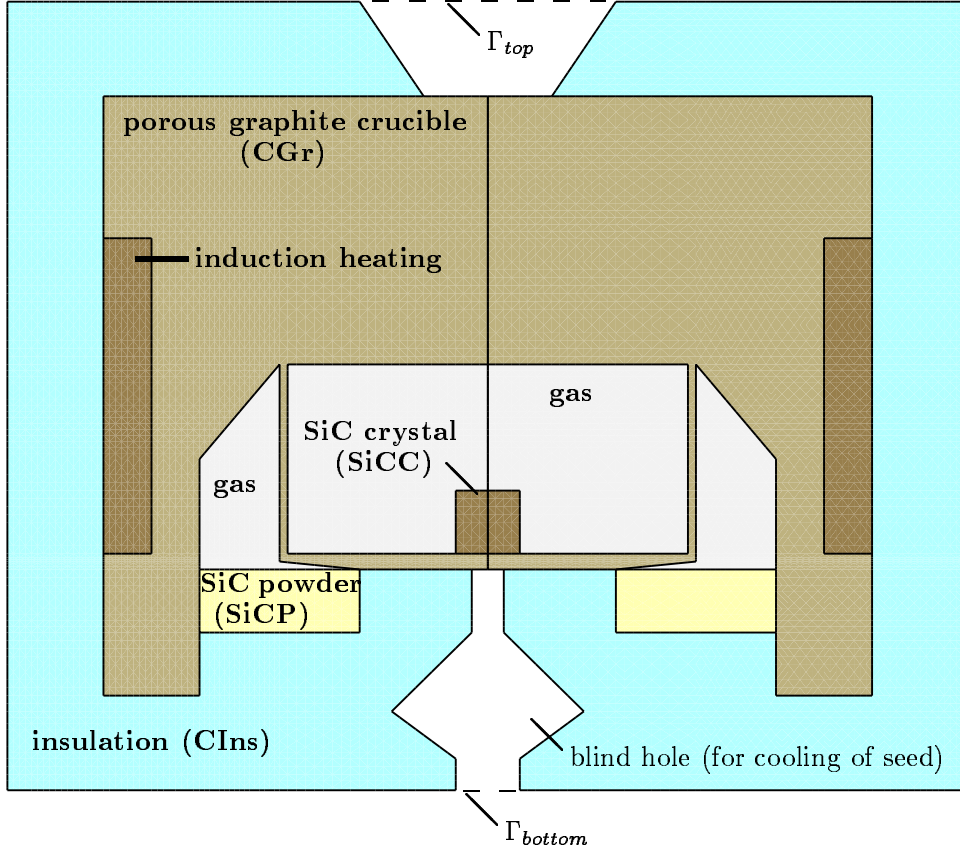


Figure 1: Set-up of growth apparatus with source powder and crystal seed in separate chambers, seed at bottom.

[BKP⁺99, (2.18a-2.18d)]:

$$\text{mass: } \frac{d\rho_{gas}}{dt} + \rho_{gas} \operatorname{div} \vec{v}_{gas} = 0, \quad (1.1a)$$

$$\text{momentum: } \rho_{gas} \frac{d\vec{v}_{gas}}{dt} + \operatorname{grad} p_{gas} = \rho_{gas} \vec{g}, \quad (1.1b)$$

$$\text{energy: } \frac{dU_{gas}}{dt} + \frac{1}{\rho_{gas}} \operatorname{div} \vec{q}_{gas} + \frac{1}{\rho_{gas}} p_{gas} \operatorname{div} \vec{v}_{gas} = r_{gas}, \quad (1.1c)$$

reaction-diffusion equations (one for each gas species α):

$$\frac{dc^{(\alpha)}}{dt} - \frac{1}{\rho_{gas}} \operatorname{div} \left(\rho_{gas} c^{(\alpha)} (D^{(\alpha)})^{-1} (\operatorname{grad} p^{(\alpha)} - c^{(\alpha)} \operatorname{grad} p_{gas}) \right) = \frac{1}{\rho_{gas}} \rho^{*(\alpha)}, \quad (1.1d)$$

where

$$\frac{d}{dt} := \frac{\partial}{\partial t} + \vec{v}_{gas} \bullet \text{grad}, \quad (1.2a)$$

$$p_{gas} = \sum_{\alpha} p^{(\alpha)}, \quad U_{gas} = \sum_{\alpha} c^{(\alpha)} U^{(\alpha)}, \quad (1.2b)$$

$$\vec{q}_{gas} = -\kappa_{gas} \text{grad } T - \sum_{\alpha} (\rho_{gas} c^{(\alpha)} U^{(\alpha)} + p^{(\alpha)}) (D^{(\alpha)})^{-1} (\text{grad } p^{(\alpha)} - c^{(\alpha)} \text{grad } p_{gas}). \quad (1.2c)$$

In equations (1.1) and (1.2) the subscript *gas* is used for quantities in the gas mixture, while superscripts (α) indicate quantities in the gas species α . The meaning of the symbols is as follows:

ρ_{gas} – mass density,	
\vec{v}_{gas} – local mean velocity of gas molecules,	
p_{gas} – total pressure,	$p^{(\alpha)}$ – partial pressure,
\vec{g} – gravity,	
U_{gas} – total internal energy,	$U^{(\alpha)}$ – partial internal energy,
$c^{(\alpha)}$ – mass concentration,	q_{gas} – heat flux,
$D^{(\alpha)}$ – diffusion coefficient,	r_{gas} – radiation,
$\rho^{*(\alpha)}$ – partial mass source (chemical reactions, phase transitions),	
κ_{gas} – thermal conductivity,	T – absolute temperature.

If the heat flux of the gas mixture is decomposed into the sum of the heat fluxes of the different contributing gas species as it was done in [BKP⁺99, (2.14c), (2.19b)], then the thermal conductivity of each species α depends on the concentrations of all other species, i.e. $\kappa^{(\alpha)} = \kappa^{(\alpha)}(c^{(\alpha_1)}, \dots, c^{(\alpha_A)}, T)$ if $\alpha_1, \dots, \alpha_A$ are all the components making up the gas mixture (cf. e.g. [CC70]). This was not unambiguously stated in [BKP⁺99, (2.14c)]. Since the introduction of the quantities $\kappa^{(\alpha)}(c^{(\alpha_1)}, \dots, c^{(\alpha_A)}, T)$ does not provide any advantages, we rather take the point of view that the total heat flux is given by (1.2c), where $\kappa_{gas} = \kappa_{gas}(c^{(\alpha_1)}, \dots, c^{(\alpha_A)}, T)$.

Equations (1.1) are furthermore coupled by the following material laws, furnished by the theory of ideal gases (cf. [BKP⁺99, (2.14*)]):

$$p^{(\alpha)} = \rho_{gas} c^{(\alpha)} \frac{R}{M^{(\alpha)}} T, \quad U^{(\alpha)} = z^{(\alpha)} \frac{R}{M^{(\alpha)}} T, \quad (1.3a)$$

$$\rho^{*(\alpha)} = \sum_{i=1}^N \gamma_i^{(\alpha)} M^{(\alpha)} \mu_H \Lambda^{(i)}, \quad (1.3b)$$

where R is the universal gas constant, $M^{(\alpha)}$ is the molecular weight, $z^{(\alpha)} = \frac{3}{2}$ for single-, $z^{(\alpha)} = \frac{5}{2}$ for double-, and $z^{(\alpha)} = 3$ for multi-atomic gas molecules, N is the number of chemical reactions and phase transitions, $\gamma_i^{(\alpha)}$ are the stoichiometric coefficients, μ_H is the hydrogen molecular weight, and $\Lambda^{(i)}$ are rates of chemical reactions or phase transitions, respectively.

Neglecting any mechanical or chemical effects inside solid parts of the growth apparatus, the model is completed by equations describing the heat conduction through the solid components of the growth apparatus (cf. [BKP⁺99, (2.20)]),

$$\rho^{[\beta]} c_{sp}^{[\beta]} \frac{\partial T}{\partial t} + \operatorname{div} \vec{q}^{[\beta]} = \rho^{[\beta]} \mu^{[\beta]}, \quad (1.4)$$

where superscripts $[\beta]$ refer to quantities in the solid component β , $\rho^{[\beta]}$ denotes mass density, $c_{sp}^{[\beta]}$ denotes specific heat, $\vec{q}^{[\beta]}$ denotes heat flux, and $\mu^{[\beta]}$ is a heat source corresponding to the induction heating. Let us remark that the specific heat functions $c_{sp}^{[\beta]}$ are the ones actually measured in physical experiments, which is in contrast to those used in [BKP⁺99, (2.20)]. The heat flux obeys

$$\vec{q}^{[\beta]} = -\kappa^{[\beta]} \operatorname{grad} T, \quad (1.5)$$

$\kappa^{[\beta]}$ denoting thermal conductivity. Equations (1.4) are coupled to the corresponding equations for the gas phase via suitable interface conditions.

Our present paper is merely concerned with the energy balance of the above model. All quantities except temperature and radiation are treated as being given, in particular, $c^{(\alpha)}$, \vec{v}_{gas} and ρ_{gas} . For this treatment, (1.2c) simplifies to

$$\vec{q}_{gas} = -\kappa_{gas} \operatorname{grad} T. \quad (1.6)$$

Two basic geometric set-ups prevail in the literature, confer e.g. [Kon95]. For the first set-up the crystal seed and the source powder are placed inside a single chamber of the growth apparatus, the seed at the top and the source at the bottom. This is the set-up that was used for the numerical simulation in [BKP⁺99]. The second set-up features two different chambers for the seed and for the source, separated by a porous graphite wall as depicted in Figure 1. Here the silicon diffuses through the pores of the graphite wall into the growth chamber, where the seed is usually at the bottom of the cavity. The second set-up will be used for the numerical experiments considered in this paper (cf. Section 3.3).

Our paper is organized as follows: In Section 2, we describe the physical model used for the radiation between the different components of the growth apparatus. In Section 3, we report on the numerical simulations, indicating the particular method used.

2 Modeling Radiation

We just give a brief summary of the physical radiation model. Confer [DNR⁺90] and [Jär96, Chapter 3.3] for further details and references.

In our treatment, we do not consider any interaction between gas and radiation. This simplification seems to be justified since the gas components making up the gas mixture do not have absorption bands in their spectra within the interesting range of temperatures. In particular, radiation is assumed to travel unperturbed between surfaces of

solid components throughout cavities inside the growth apparatus. All solids except the SiC single crystal are treated as being opaque. For the SiC single crystal we account for semi-transparency using the energy-band model.

We are first going to describe the opaque case, and subsequently, we will indicate modifications due to semi-transparency.

In the opaque case no radiation is transmitted through a solid surface. Hence, at any point \vec{x} of a solid surface the areal power density of the total outgoing radiation is given by

$$S(\vec{x}) = E(\vec{x}) + R(\vec{x}), \quad (2.1)$$

where $E(\vec{x})$ is the contribution due to emittance and $R(\vec{x})$ is the contribution due to reflection.

Reflection and emittance are supposed to be diffuse-gray, i.e. independent of the angle of incidence, as well as of the wavelength.

According to the Stefan-Boltzmann law, it holds that

$$E(\vec{x}) = \sigma \varepsilon(\vec{x}, T(\vec{x})) T^4(\vec{x}), \quad (2.2)$$

where $\sigma = 5.670 \cdot 10^{-8} \frac{\text{W}}{\text{m}^2 \text{K}^4}$ is the Boltzmann radiation constant and ε is the emissivity of the surface, depending on the position \vec{x} and the absolute temperature T at \vec{x} .

The reflective term can be expressed using the reflectivity $\varrho(\vec{x}, T(\vec{x}))$, i.e. the ratio between reflected and incoming radiation, and the areal density of the power of the incoming radiation $\mathcal{J}(S)(\vec{x})$:

$$R(\vec{x}) = \varrho(\vec{x}, T(\vec{x})) \mathcal{J}(S)(\vec{x}). \quad (2.3)$$

Kirchhoff's law yields that the absorptivity of a surface, i.e. the ratio between absorbed and incoming radiation, is equal to its emissivity. Consequently,

$$\varrho(\vec{x}, T(\vec{x})) = 1 - \varepsilon(\vec{x}, T(\vec{x})). \quad (2.4)$$

Due to diffuseness, \mathcal{J} can be calculated using the integral operator defined by

$$\mathcal{J}(S)(\vec{x}) = \int_{\Gamma} \Lambda(\vec{x}, \vec{y}) \omega(\vec{x}, \vec{y}) S(\vec{y}) d\vec{y}. \quad (2.5)$$

Here, Γ consists of the union of all surfaces of solid components adjacent to the considered cavity. For \vec{x}, \vec{y} on Γ , the *visibility factor* Λ equals 0 if the view between points \vec{x} and \vec{y} is blocked, and Λ equals 1 otherwise. The *view factor* ω is given as

$$\omega(\vec{x}, \vec{y}) = \frac{\vec{n}_{gas}(\vec{y}) \bullet (\vec{x} - \vec{y}) \vec{n}_{gas}(\vec{x}) \bullet (\vec{y} - \vec{x})}{\pi ((\vec{y} - \vec{x}) \bullet (\vec{y} - \vec{x}))^2}, \quad (2.6)$$

where \vec{n}_{gas} is the unit normal vector on Γ pointing from gas to solid.

Combining equations (2.1) through (2.5) results in the following non-local equation for S :

$$S(\vec{x}) - (1 - \varepsilon(\vec{x}, T(\vec{x}))) \mathcal{J}(S)(\vec{x}) = \sigma \varepsilon(\vec{x}, T(\vec{x})) T^4(\vec{x}). \quad (2.7)$$

Accordingly, the areal power density of radiation is included in the interface conditions between solid and gas and introduces a non-local coupling into the energy balance. If the respective locations of all solid components of the growth apparatus do not change with time, the resulting interface condition between the solid β and the gas phase reads

$$\vec{q}_{gas} \bullet \vec{n}_{gas} - S + \mathcal{J}(S) = \vec{q}^{[\beta]} \bullet \vec{n}_{gas}. \quad (2.8)$$

The remaining part of the section is dedicated to a short description of the energy-band model of semi-transparency.

According to this model, the spectrum decomposes into a *reflective* band of wavelengths I_r and a *transmittive* band of wavelengths I_t . Radiation corresponding to I_r interacts with the surface of the semi-transparent material, i.e. it is emitted, reflected and absorbed by the surface. Radiation corresponding to I_t does not interact with the material at all, i.e. it is transmitted unperturbed through the medium. Thus, the energy-band model neglects radiation transmitted between the interior and the exterior of the semi-transparent material. This is an accurate approximation if the fraction of the power density stemming from wavelengths, where the spectral optical thickness of the semi-transparent medium is close to one is sufficiently small (cf. [DNR⁺90, Sec. 3.4]). Radiation-driven heat transport staying inside a solid component is assumed to be accounted for by the corresponding temperature dependent law of thermal conductivity.

The contributions from the two energy bands are computed separately. While the radiation region for the reflective band consists of the actual cavity, the radiation region for the transmittive band is made up of the cavity united with the semi-transparent body. Consequently, the boundary Γ_t of the transmittive radiation region is different from the boundary Γ from the opaque case, Γ_t containing the interfaces between semi-transparent material and opaque solids instead of interfaces between semi-transparent body and gas.

On Γ let S_r , E_r and R_r denote the respective contributions to the areal power density stemming from wavelengths in the reflective band I_r , corresponding to the quantities S , E and R from the opaque case. These quantities satisfy (2.1), while Planck's law of black body radiation yields that for E_r the emissivity ε written in (2.2) has to be replaced by

$$\varepsilon_r(\vec{x}, T(\vec{x})) := \int_{I_r} \varepsilon(\vec{x}, T(\vec{x}), \lambda) \frac{15C^4}{\pi^4 \lambda^5 T^4(\vec{x}) \left(e^{\frac{C}{\lambda T(\vec{x})}} - 1 \right)} d\lambda, \quad (2.9)$$

where $C = 1.4388 \cdot 10^{-2} \text{m K}$ and $\varepsilon(\vec{x}, T(\vec{x}), \lambda)$ is the emissivity for monochromatic radiation of wavelength λ .

Moreover, using Planck's and Kirchhoff's laws to determine the absorptivity of Γ with respect to the reflective band, (2.3) also holds for S_r and R_r , if $\rho(\vec{x}, T(\vec{x}))$ is replaced

by

$$\varrho_r(\vec{x}, T(\vec{x})) = 1 - \varepsilon(\vec{x}, T(\vec{x})) \left(\int_{I_r} \frac{15C^4}{\pi^4 \lambda^5 T^4(\vec{x}) \left(e^{\frac{c}{\lambda T(\vec{x})}} - 1 \right)} d\lambda \right)^{-1}. \quad (2.10)$$

As in the opaque case, one can now derive a non-local equation for S_r , similar to (2.7).

Letting S_t , E_t , R_t , ε_t and ϱ_t denote the quantities with respect to the transmissive band, corresponding to S_r , E_r , R_r , ε_r and ϱ_r , respectively, the procedure to compute the transmissive contributions is analogous to the reflective case, using Γ_t instead of Γ . \mathcal{J}_t will denote the operator corresponding to \mathcal{J} with Γ replaced by Γ_t ; ε_t and ϱ_t are computed by replacing I_r with I_t in both (2.9) and (2.10).

At points between gas and opaque solids, i.e. at points from the set $\Gamma_t \cap \Gamma$, one obtains contributions from both bands I_r and I_t , which then are incorporated additively into the corresponding interface condition, which results in an equation of the form (2.8) with $-S + \mathcal{J}(S)$ replaced by $-S_r + \mathcal{J}(S_r) - S_t + \mathcal{J}_t(S_t)$.

On interfaces between gas and semi-transparent medium, i.e. on $\Gamma \setminus \Gamma_t$, only contributions from the reflective band are obtained, such that one has (2.8) with S_r instead of S . Analogously, on $\Gamma_t \setminus \Gamma$, i.e. on interfaces between semi-transparent solids and opaque solids, only transmissive contributions are present. Hence, the interface condition between an opaque solid β and a semi-transparent solid γ reads

$$\vec{q}^{[\gamma]} \bullet \vec{n}_\gamma - S_t + \mathcal{J}_t(S_t) = \vec{q}^{[\beta]} \bullet \vec{n}_\gamma, \quad (2.11)$$

where \vec{n}_γ is the unit normal vector on the interface pointing from material γ to material β .

3 Numerical Simulation

3.1 Setting

For the numerical simulation we follow a similar approach as in [BKP⁺99]. We take into account the cylindrical symmetry of the growth apparatus, and we assume that ρ_{gas} and \vec{v}_{gas} only vary with respect to the vertical coordinate, all non-vertical components of \vec{v}_{gas} being zero. Moreover, we recall that the radiation model of the preceding section assumes that there are no radiating or absorbing particles inside the gas phase.

Applying the energy balance of the gas phase (1.1c) to the situation at hand, multiplying by ρ_{gas} , using (1.6) and writing the result in cylindrical coordinates (r, z) , one arrives at

$$\rho_{gas} \frac{\partial U_{gas}}{\partial t} + (\vec{v}_{gas})_z \rho_{gas} \frac{\partial U_{gas}}{\partial z} - \text{div}(\kappa_{gas} \text{grad } T) + p_{gas} \frac{\partial (\vec{v}_{gas})_z}{\partial z} = 0, \quad (3.1)$$

where p_{gas} and U_{gas} are given by (1.2b) in combination with (1.3a).

Some problems arise from the fact that we use a given velocity distribution to model convective heat transport. In the case that porosity is high in most of the solid parts of the growth apparatus, it is a reasonable first approximation to consider a constant field for \vec{v}_{gas} inside the whole apparatus. Neglecting the fact that compared to pure gas regions the gas speed will increase and ρ_{gas} will decrease inside porous media is justified, since inside porous domains the diffusive heat transfer through the gas phase is negligible against the diffusive heat transfer through the solid phase. The convective heat transfer (cf. (3.1)) is not affected by our approximation, since due to mass conservation the product $\rho_{gas} \vec{v}_{gas}$ must be constant throughout the growth apparatus. This approach does not account for any inhomogeneity in the porosity of solid components.

In the case that one has to deal with interfaces between gas cavities and non-porous solids, one has to impose $\vec{v}_{gas} = 0$ on such interfaces. Therefore, one cannot prescribe a non-vanishing velocity field which is constant. To guarantee consistency of such a velocity distribution, one had to solve the mass and momentum balance equations. Since this is not in the scope of this article, we restrict ourselves to the abovementioned case of high porosity.

The energy balance inside the skeleton of the solid component β is provided by (1.4). For the simulations of this paper we assume that the heat source is distributed uniformly over some domain, where the induction coils couple to the growth apparatus (cf. Fig. 1). To improve the accuracy of the simulation of the induction heating, it is desirable to determine the distribution of the heat source by numerically solving Maxwell's equations in future work.

The complete energy balance for the spatial domain of the solid component β can be written in the approximate form

$$\begin{aligned} \rho_{gas} \frac{\partial U_{gas}}{\partial t} + (\vec{v}_{gas})_z \rho_{gas} \frac{\partial U_{gas}}{\partial z} - \text{div}(\kappa_{gas} \text{grad } T) \\ + \rho^{[\beta]} c_{sp}^{[\beta]} \frac{\partial T}{\partial t} + \text{div} \vec{q}^{[\beta]} = \rho^{[\beta]} \mu^{[\beta]}, \end{aligned} \quad (3.2)$$

which follows from addition of equations (3.1) and (1.4) and from the assumed constancy of \vec{v}_{gas} .

It is assumed that the temperature is continuous throughout the growth apparatus. On interfaces between gas-cavities and solid domains, equations (3.1) and (3.2) are coupled by the interface conditions (2.8). On interfaces between different solid materials, the heat flux is either continuous or, if one of the solids is semi-transparent, it obeys (2.11).

Finally, the ambient environment of the growth apparatus is assumed to radiate at room temperature T_{room} with some appropriate average emissivity $\bar{\epsilon}$. Thus outer boundaries emit according to the Stefan-Boltzmann law

$$\vec{q}^{[\beta]} \bullet \vec{n}_\beta = \sigma (\epsilon^{[\beta]}(T) T^4 - \bar{\epsilon} T_{room}^4), \quad (3.3)$$

and we use phantom closures of open radiation regions such as Γ_{top} and Γ_{bottom} depicted in Figure 1 which radiate at room temperature, but do not absorb or reflect radiation.

3.2 Method

The time discretization is fully implicit except for the emissivity, where the temperature of the preceding time step is taken. The discretized version of (2.8) is then used in the finite volume scheme for (3.1) and (3.2). As in [BKP⁺99], the utilized finite volume method consists of a slightly modified version of the one presented in [Fuh97]. The discrete scheme has been implemented using the PDELIB program package, being developed at the Weierstrass Institute of Applied Analysis and Stochastics, Berlin (cf. [FKL98]).

All interfaces are supposed to be piecewise linear. The line segments that the interfaces between radiation regions and ambient solids are made up of, will be called *radiation edges*. Hence, radiation edges are the boundary elements making up the sets Γ and Γ_t from Section 2.

Computing the discretized radiation terms involves the evaluation of integrals of the form

$$\lambda_{Z,W} := \int_Z \int_W \Lambda^*((r,z), (s,y)) s \, d(s,y) r \, d(r,z), \quad (3.4)$$

where W and Z are one-dimensional boundary elements of the respective radiation region. None of these boundary elements is to contain any corners or material interfaces in its interior. Notice that all regions are now two-dimensional due to cylindrical symmetry. The integrated view factor Λ^* reads

$$\Lambda^*((r,z), (s,y)) = 2 \int_0^\pi \Lambda((r,0,z), (s \cos(\tau), s \sin(\tau), y)) \omega((r,0,z), (s \cos(\tau), s \sin(\tau), y)) \, d\tau. \quad (3.5)$$

It is defined on radiation edges except for their corner points. Even though the points in the argument of Λ^* are only two-dimensional, the visibility factor Λ and the view factor ω still have to be computed in three dimensions. Their arguments are hence written in cartesian coordinates.

We evaluate the integrated view factors following the treatment in [DNR⁺90]. The idea of the method presented therein is to use an algorithm that is provided with two points (r,z) and (s,y) on the boundary of a gas enclosure, none of the points coinciding with a corner, returning the lower and upper limits of the angle intervals, where the two points are mutually visible. In other words, the algorithm determines the intervals I such that $\tau \in I$ implies $\Lambda((r,0,z), (s \cos(\tau), s \sin(\tau), y)) = 1$.

For any radiation region the algorithm runs through the list of adjacent radiation edges and for each radiation edge g it computes the angle interval for which the view is blocked by g according to the procedure that is presented in [DNR⁺90] in some detail.

It then remains to piece the intervals together. To this end, the following observations can be helpful. The boundary of each radiation region decomposes into one or more connected components. Owing to rotational symmetry, it is assumed that radiation regions ambient to the $r = 0$ line are reflected through that line, so that e.g. the

boundary of region R_1 in Fig. 2 is closed. In the case that all connected components are closed, there is a unique connected component C_{out} containing all others in its interior (cf. regions R_1 and R_2 in Fig. 2). It can also occur that there are connected components that are not closed. In this case C_{out} denotes the union of all such connected components (cf. Fig. 2, region R_3).

The set of angles blocked by C_{out} must have the form $[0, \tau_{min}]$ or $[\tau_{max}, \pi]$ or $[0, \tau_{min}] \cup [\tau_{max}, \pi]$, where $0 \leq \tau_{min} \leq \tau_{max} \leq \pi$. The same is true for all connected components containing at least one of the points under consideration. For all other connected components C the set of angles blocked by C can also be of the form $[\tau_{min}, \tau_{max}]$.

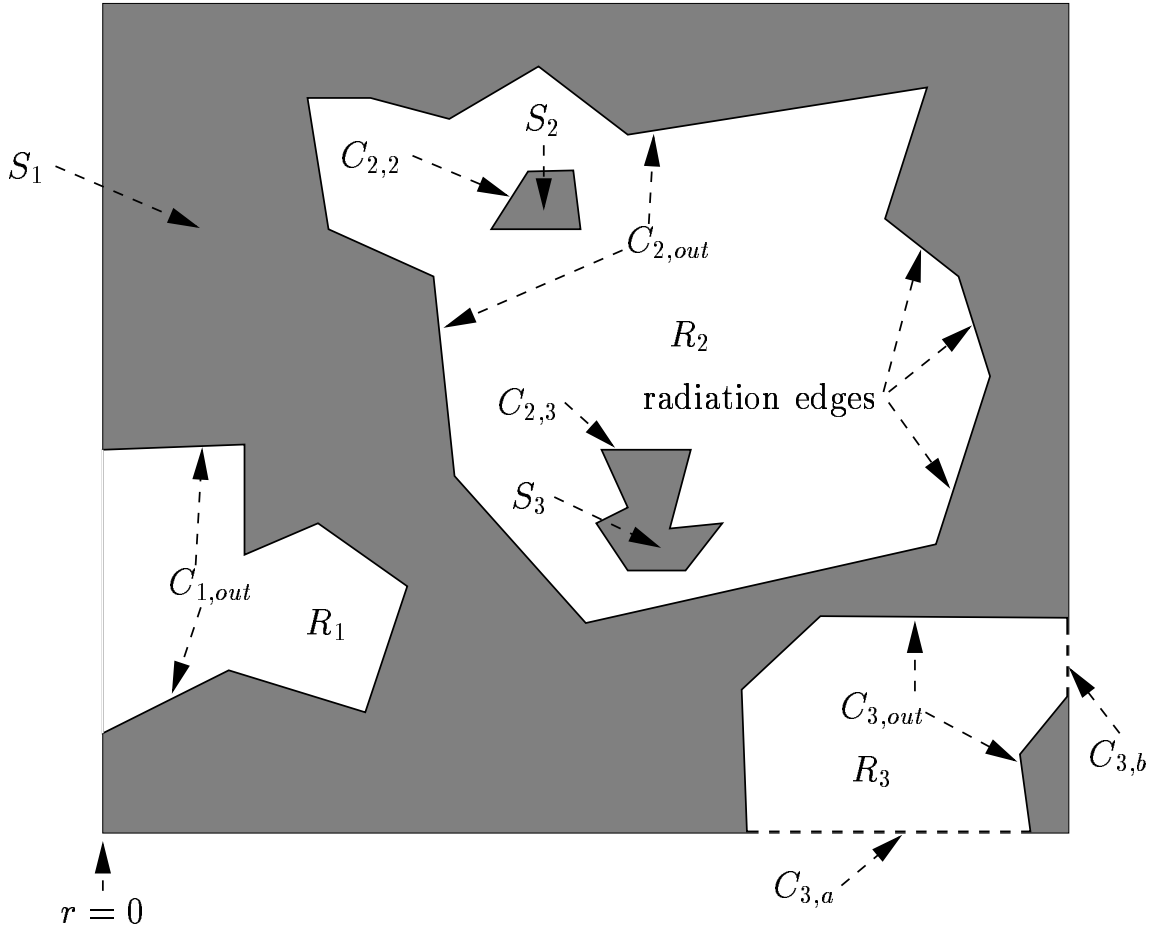


Figure 2: Radiation regions R_1 , R_2 , R_3 together with adjacent solid domains S_1 , S_2 , S_3 . While the boundary of R_1 consists of just one connected component $C_{1,out}$, the boundary of R_2 has three connected components $C_{2,out}$, $C_{2,2}$, $C_{2,3}$, where $C_{2,out}$ contains $C_{2,2}$ and $C_{2,3}$ in its interior. $C_{3,out}$ consists of two connected components, which are not closed, $C_{3,a}$ and $C_{3,b}$ indicate an artificial closure, similar to Γ_{top} and Γ_{bottom} in Fig. 1.

Moreover, if one considers the radiation edges belonging to the same connected component in consecutive order, after the initial one, each additional radiation edge decreases

a visibility interval either from above or from below or not at all.

One still has to combine the intervals resulting from the different connected components, but in general there will be considerably less connected components than radiation edges.

Since in the cylindrically symmetric case the antiderivative of ω is known analytically (cf. [DNR⁺90, (24)]), one now is in the position to compute Λ^* . The evaluation of the terms (3.4) can then be completed by numerical integration methods. As mentioned in [DNR⁺90, Section 3.3], one has to use care when applying Gaussian quadrature to determine the integrals (3.4), since Λ^* has points of discontinuity. To verify the accuracy of the numerical computation, one can use the identity

$$\int_{\partial R} \Lambda^*((r, z), (s, y)) s \, d(s, y) = 1 \quad (3.6)$$

that holds for each closed radiation region R and for each point (r, z) on its boundary ∂R . To make (3.6) usable for open radiation regions, one can introduce artificial closures as indicated by the dashed lines in Fig. 2. This is the same concept as the phantom closures Γ_{top} and Γ_{bottom} discussed at the end of Sec. 3.1 and depicted in Fig. 1. In the code that was implemented for the numerical simulations presented in this paper we used

$$\int_Z r \, d(r, z) = \sum_{W \subseteq \partial R} \lambda_{Z,W}, \quad (3.7)$$

holding for every boundary element Z of R , to calculate the relative error in the numerical integration. (3.7) is an immediate consequence of (3.4) and (3.6). The algorithm increases the number of points used in the Gaussian quadrature until the relative error falls below a prescribed precision. For the numerical experiments of Section 3.3 this precision was set to 10^{-5} . Moreover, if Σ denotes the numerical value for the right-hand side of (3.7), then we substitute each $\lambda_{Z,W}$ by $\lambda_{Z,W} \cdot \int_Z r \, d(r, z) / \Sigma$ in order to guarantee that energy conservation is satisfied exactly.

3.3 Numerical Experiments

Since the material data can vary considerably even between two different growth cycles occurring in the same growth apparatus, it is not feasible to exactly simulate one specific run of a growth experiment. We therefore aim at simulating an idealized growth apparatus, using typical material data where available. The material data that have been used during the following numerical experiments are listed in Appendix A.

All numerical experiments have been done for a gas phase consisting of pure argon, i.e. using $c^{(Ar)} = 1$. It is known from measurements that, for temperatures greater than 2500 K, gas species such as Si, Si₂C and SiC₂ make up a significant portion of the gas mixture (cf. [ABEP98, Fig. 10]). Even so, the error from taking only Ar into account should not be too large, since for lower temperatures only Ar is present in the gas phase, and for higher temperatures heat is mainly transported via radiation.

We discuss four numerical experiments demonstrating the respective influence of radiative and convective heat transfer inside a growth apparatus of height 0.25 m and radius 0.15 m. Each experiment starts at 293 K. The system is then heated inside the rectangular area labeled with “induction heating” in Figure 1 using a constant heating power of 10 kW. Figures 3 and 4 show three temporal snapshots of the temperature distribution evolution of each experiment, the first at 300 s, the second at 3000 s and the third at 30000 s, when the simulations have reached a quasi-stationary state. Each column belongs to the same experiment. The experiments will be referred to as R/NC (Figure 3, left column), R/C (Figure 3, right column), NR/NC (Figure 4, left column) and NR/C (Figure 4, right column).

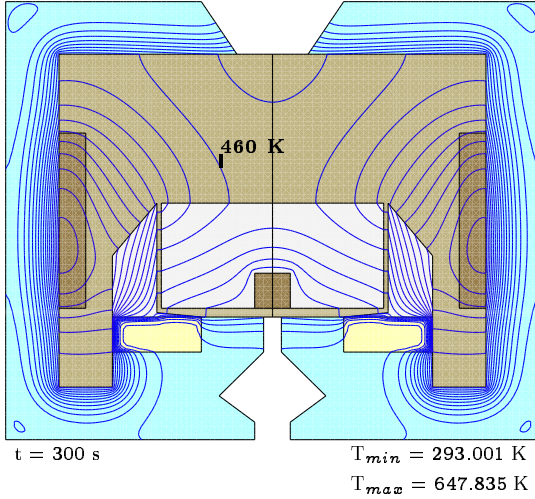
R/NC and NR/NC contain no convective heat transport, using $\vec{v}_{gas} = 0$, whereas $(\vec{v}_{gas})_z$ was set to -10 m/s in R/C and NR/C, gas streaming from top to bottom. In contrast to R/NC and R/C, experiments NR/NC and NR/C do *not* take into account radiative heat transport inside the cavities labeled with “gas” in Figure 1 and neither inside the two blind holes. Instead, emitting boundary conditions are used in NR/NC and NR/C at all boundary faces of the upper blind hole and at the horizontal boundary face of the lower blind hole (see faces labeled “ Γ_{em} ” in the upper right picture of Fig. 4).

The minimal temperature T_{min} does always occur at the outside of the outer insulation layer of the apparatus, where the isolines become extremely dense at higher temperatures, appearing as a uniformly dark area in the last two stages of Figures 3 and 4. T_{max} does always occur inside the rectangular heating region. Since the temperature difference between neighboring isolines is 20 K, the pictures allow to determine the temperature in most of the apparatus.

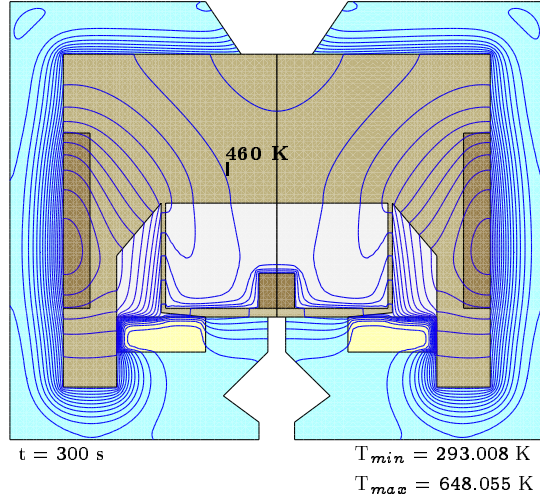
In agreement with physical expectations, the convection pushes the isolines in its moving direction, especially in pure gas regions and where \vec{v}_{gas} is perpendicular to the isolines, resulting in steeper temperature gradients at the lower rim of the growth chamber. This effect becomes less prominent at higher temperatures, where radiative heat transfer is more powerful (cf. R/NC and R/C, stages 2 and 3). By comparing the temperature labels provided in Figures 3 and 4, one notices a cooling effect of the flowing gas, resulting e.g. in a temperature difference of some 20 K at the crystal surface between R/NC and R/C.

A comparison of the second and third stages of R/NC and R/C with the second and third stages of NR/NC and NR/C illustrates that it is of the utmost importance to take radiative heat transport in the cavities into account in order to find a realistic temperature distribution. Neglecting radiation results in unphysically large heat gradients inside the growth chamber and at the crystal surface, where the temperature should actually be almost homogeneous (cf. R/NC, stage 3 and R/C stage 3 in Figure 3).

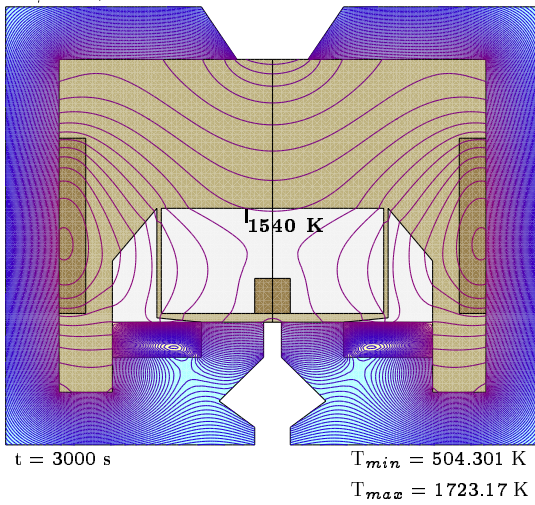
R/NC, state 1



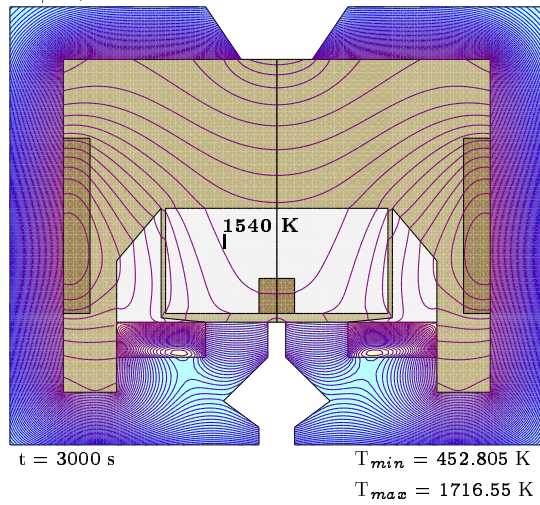
R/C, state 1



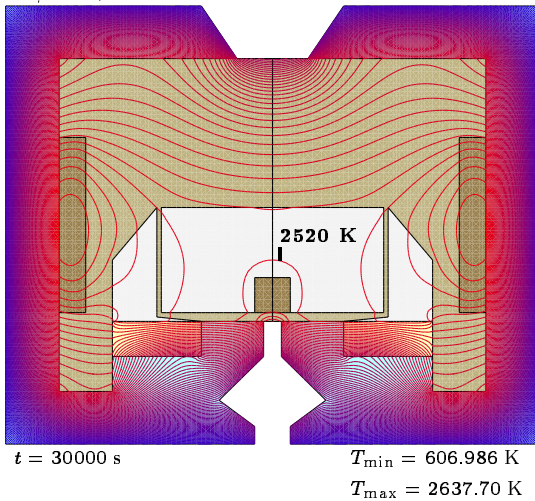
R/NC, state 2



R/C, state 2



R/NC, state 3



R/C, state 3

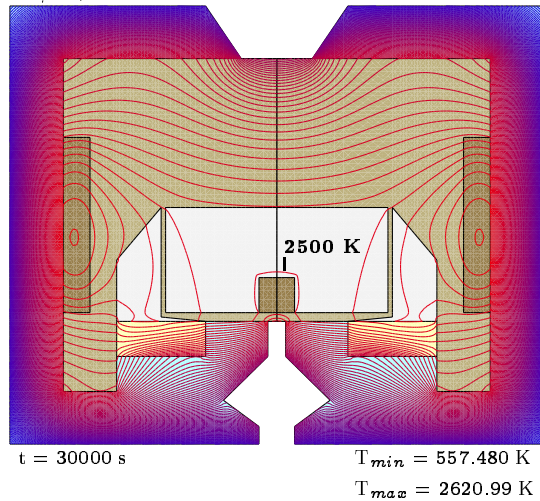
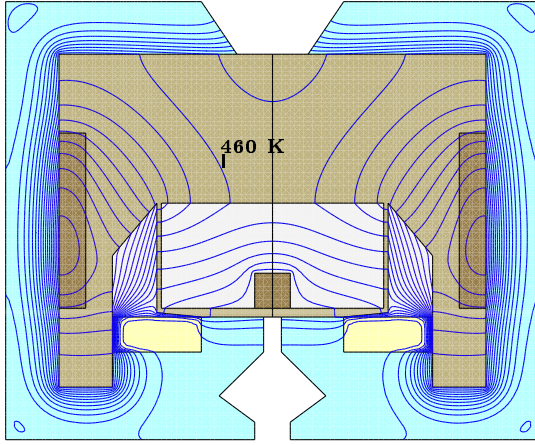


Figure 3: Left-hand column: simulation with radiation, no convection. Right-hand column: simulation with radiation and downward convection. Temperature difference between neighboring isolines is 20 K.

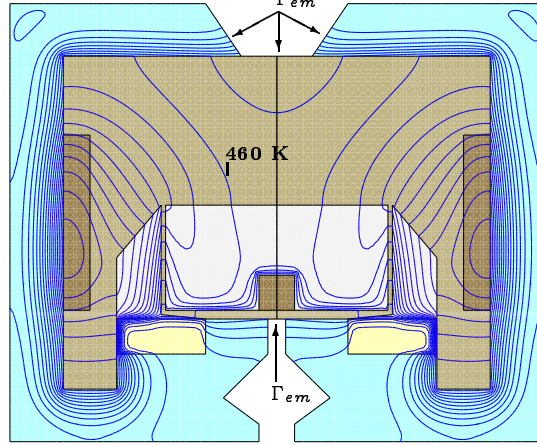
NR/NC, state 1



t = 300 s

 $T_{min} = 293.001 \text{ K}$
 $T_{max} = 648.936 \text{ K}$

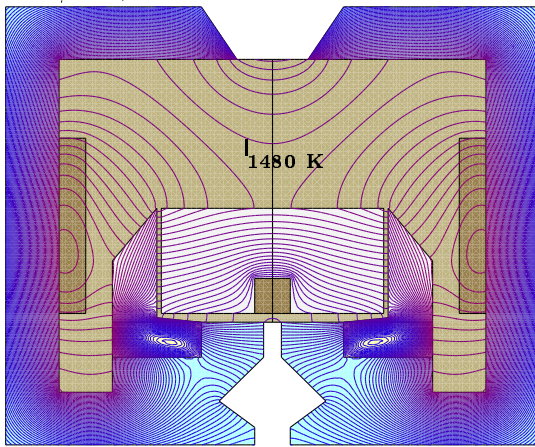
NR/C, state 1



t = 300 s

 $T_{min} = 293.007 \text{ K}$
 $T_{max} = 649.138 \text{ K}$

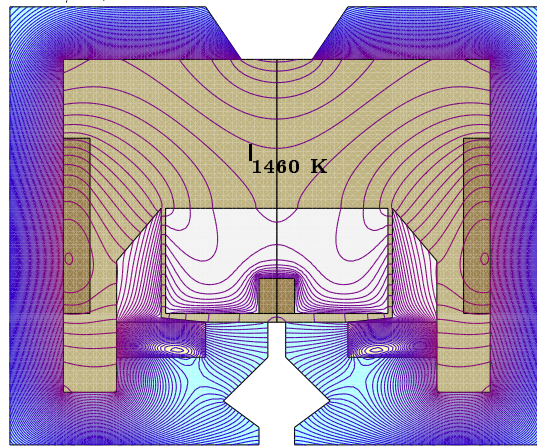
NR/NC, state 2



t = 3000 s

 $T_{min} = 479.552 \text{ K}$
 $T_{max} = 1746.90 \text{ K}$

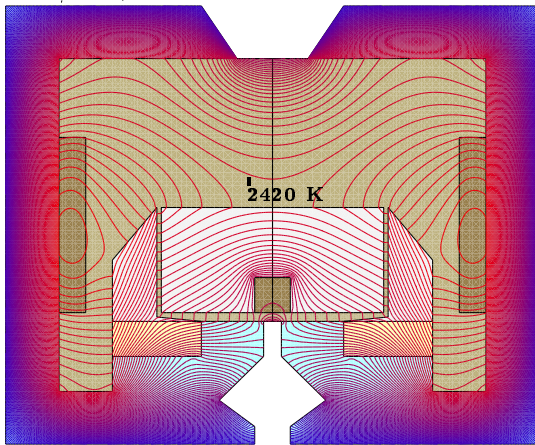
NR/C, state 2



t = 3000 s

 $T_{min} = 452.905 \text{ K}$
 $T_{max} = 1740.54 \text{ K}$

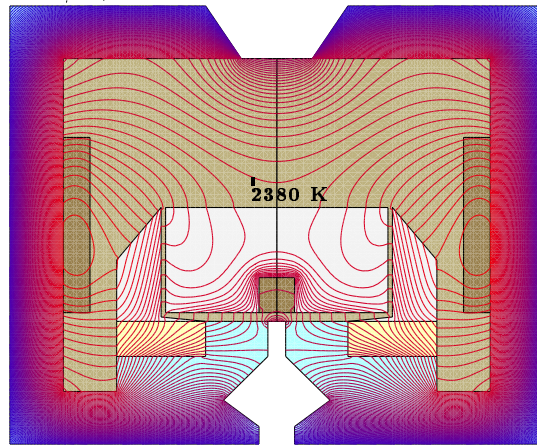
NR/NC, state 3



t = 30000 s

 $T_{min} = 606.440 \text{ K}$
 $T_{max} = 2652.82 \text{ K}$

NR/C, state 3



t = 30000 s

 $T_{min} = 555.661 \text{ K}$
 $T_{max} = 2636.09 \text{ K}$

Figure 4: Left-hand column: simulation without radiation, no convection. Right-hand column: simulation without radiation and with downward convection. Temperature difference between neighboring isolines is 20 K.

4 Conclusions

The numerical experiments of the preceding section agree with physical expectations, supporting the reliability of the presented numerical model and of the employed numerical algorithms, which at the current stage provide an effective tool to test different geometrical set-ups as well as vertical convection with respect to their influence on the resulting temperature evolution inside the growth apparatus. Including radiative heat transport through cavities was an essential step to achieve results of satisfactory accuracy.

From the results of experiments R/NC and R/C presented in Section 3.3, one can conclude that for a highly porous growth apparatus one can achieve significant changes in the shape and magnitude of the temperature distribution inside the growth chamber by regulating the amount of inert gas pumped into the reactor, indicating that inert gas convection can be an important control parameter.

A Appendix: Material Data

In order to guarantee the satisfactory performance of the numerical algorithms used in the simulations, it was necessary to ensure that the different segments of piecewise defined functions are fitted together sufficiently smooth. This is the cause for the large number of digits in some of the following coefficients which is not to indicate that the physical values are known with such accuracy.

A.1 Gas Phase

Using $\rho_{gas} = 3.73 \cdot 10^{-3} \frac{\text{kg}}{\text{m}^3}$, $M^{(\text{Ar})} = 39.9 \cdot 10^{-3} \frac{\text{kg}}{\text{mol}}$, $z^{(\text{Ar})} = 1.5$, it remains to provide the thermal conductivity $\kappa_{gas} = \kappa^{(\text{Ar})}$. For $\kappa^{(\text{Ar})}$ we refer to [Var75, p. 561] which has been used to fit $\kappa^{(\text{Ar})}$ as written in (A.1) below.

$$\kappa^{(\text{Ar})}(T) = \begin{cases} 1.83914 \cdot 10^{-4} \frac{\text{W}}{\text{m K}} \left(\frac{T}{\text{K}}\right)^{0.800404} & \text{for } T \leq 500 \text{ K,} \\ f_{\kappa}^{(\text{Ar})} \frac{\text{W}}{\text{m K}} \left(\frac{T}{100\text{K}}\right)^5 + e_{\kappa}^{(\text{Ar})} \frac{\text{W}}{\text{m K}} \left(\frac{T}{100\text{K}}\right)^4 + d_{\kappa}^{(\text{Ar})} \frac{\text{W}}{\text{m K}} \left(\frac{T}{100\text{K}}\right)^3 \\ \quad + c_{\kappa}^{(\text{Ar})} \frac{\text{W}}{\text{m K}} \left(\frac{T}{100\text{K}}\right)^2 + b_{\kappa}^{(\text{Ar})} \frac{\text{W}}{\text{m K}} \left(\frac{T}{100\text{K}}\right) \\ \quad + a_{\kappa}^{(\text{Ar})} \frac{\text{W}}{\text{m K}} & \text{for } 500 \text{ K} \leq T \leq 600 \text{ K,} \\ 4.19440 \cdot 10^{-4} \frac{\text{W}}{\text{m K}} \left(\frac{T}{\text{K}}\right)^{0.671118} & \text{for } T \geq 600 \text{ K} \end{cases} \quad (\text{A.1})$$

where

$$\begin{aligned} a_{\kappa}^{(\text{Ar})} &= -7.1287382681160803, & b_{\kappa}^{(\text{Ar})} &= 6.610288591812101, \\ c_{\kappa}^{(\text{Ar})} &= -2.440839830308151325, & d_{\kappa}^{(\text{Ar})} &= 0.4497633940115560911, \\ e_{\kappa}^{(\text{Ar})} &= -0.0413251721439221090, & f_{\kappa}^{(\text{Ar})} &= 0.001514463800685296. \end{aligned} \quad (\text{A.2})$$

A.2 Solid Domains

The growth apparatus used to conduct the numerical experiments of Section 3.3 employs the following solid components: A porous graphite crucible referred to as “CGr”, graphite felt for insulation referred to as “CIns”, silicon carbide source powder referred to as “SiCP”, and the silicon carbide single crystal referred to as “SiCC” (see Fig. 1).

For each solid material β one needs the following potentially temperature dependent functions: density $\rho^{[\beta]}(T)$, thermal conductivity $\kappa^{[\beta]}(T)$, specific heat $c_p^{[\beta]}(T)$ and emissivity $\varepsilon^{[\beta]}(T)$.

For the emissivity of the space ambient to the growth apparatus we have used $\bar{\varepsilon} = 0.7$.

A.2.1 Graphite Crucible

$$\rho^{[\text{CGr}]}(T) = 1750 \frac{\text{kg}}{\text{m}^3}, \quad (\text{A.3a})$$

$$\kappa^{[\text{CGr}]}(T) = 37.7158 \frac{\text{W}}{\text{m K}} e^{-1.96095 \cdot 10^{-4} \frac{T}{\text{K}}}, \quad (\text{A.3b})$$

$$c_p^{[\text{CGr}]}(T) = \frac{\frac{\text{J}}{\text{kg K}}}{441.12 \left(\frac{T}{\text{K}}\right)^{-2.30676} + 7.97093 \cdot 10^{-4} \left(\frac{T}{\text{K}}\right)^{-6.65256 \cdot 10^{-2}}}, \quad (\text{A.3c})$$

$$\varepsilon^{[\text{CGr}]}(T) = \begin{cases} 0.67 & \text{for } T \leq 1200 \text{ K,} \\ e_\varepsilon^{[\text{CGr}]} \left(\frac{T}{\text{K}}\right)^4 + d_\varepsilon^{[\text{CGr}]} \left(\frac{T}{\text{K}}\right)^3 + c_\varepsilon^{[\text{CGr}]} \left(\frac{T}{\text{K}}\right)^2 & \text{for } 1200 \text{ K} \leq T \leq 2200 \text{ K,} \\ + b_\varepsilon^{[\text{CGr}]} \left(\frac{T}{\text{K}}\right) + a_\varepsilon^{[\text{CGr}]} & \\ 0.79 & \text{for } T \geq 2200 \text{ K} \end{cases} \quad (\text{A.3d})$$

where $a_\varepsilon^{[\text{CGr}]} = \frac{46901}{125} \cdot 10^{-2}$, $b_\varepsilon^{[\text{CGr}]} = -\frac{1859}{25} \cdot 10^{-4}$, $c_\varepsilon^{[\text{CGr}]} = \frac{19249}{3} \cdot 10^{-9}$, $d_\varepsilon^{[\text{CGr}]} = -\frac{701}{3} \cdot 10^{-11}$, $e_\varepsilon^{[\text{CGr}]} = \frac{37}{12} \cdot 10^{-13}$.

$\rho^{[\text{CGr}]}$ is according to [MSS99]. $\kappa^{[\text{CGr}]}$ and $\varepsilon^{[\text{CGr}]}$ have been fitted according to Tables 1 and 2, respectively. Since [Lid95, p. 10-297] states that the range of emissivity of graphite is between 0.7 and 0.8 if $0 \leq T \leq 3600$ K, it seems reasonable to extrapolate Table 2 by a constant function for low and high temperatures. $c_p^{[\text{CGr}]}$ has been fitted according to the data in [BK73, p. 209].

$T[\text{K}]$	1000	1200	1400	1600	1800	2000	2200
$\kappa^{[\text{CGr}]} \left[\frac{\text{W}}{\text{m K}} \right]$	31.0	29.5	28.5	27.0	26.5	25.5	24.5

Table 1: Thermal conductivity of graphite crucible according to [MSS99].

T [K]	1200	1400	1600	1800	2000	2200
ε	0.67	0.69	0.73	0.76	0.77	0.79

Table 2: Emissivity of graphite crucible according to [MSS99].

A.2.2 Graphite Felt Insulation

$$\rho^{[\text{CIns}]}(T) = 170 \frac{\text{kg}}{\text{m}^3}, \quad (\text{A.4a})$$

$$\kappa^{[\text{CIns}]}(T) = \begin{cases} \left(8.1759 \cdot 10^{-2} + 2.48571 \cdot 10^{-4} \frac{T}{\text{K}} \right) \frac{\text{W}}{\text{m K}} & \text{for } T \leq 1473 \text{ K}, \\ f_{\kappa}^{[\text{CIns}]} \frac{\text{W}}{\text{m K}} \left(\frac{T}{\text{K}} \right)^5 + e_{\kappa}^{[\text{CIns}]} \frac{\text{W}}{\text{m K}} \left(\frac{T}{\text{K}} \right)^4 + d_{\kappa}^{[\text{CIns}]} \frac{\text{W}}{\text{m K}} \left(\frac{T}{\text{K}} \right)^3 \\ \quad + c_{\kappa}^{[\text{CIns}]} \frac{\text{W}}{\text{m K}} \left(\frac{T}{\text{K}} \right)^2 + b_{\kappa}^{[\text{CIns}]} \frac{\text{W}}{\text{m K}} \left(\frac{T}{\text{K}} \right) & \text{for } 1473 \text{ K} \leq T \leq 1873 \text{ K}, \\ \quad + a_{\kappa}^{[\text{CIns}]} \frac{\text{W}}{\text{m K}} & \text{for } 1473 \text{ K} \leq T \leq 1873 \text{ K}, \\ \left(-0.74475 + 7.5 \cdot 10^{-4} \frac{T}{\text{K}} \right) \frac{\text{W}}{\text{m K}} & \text{for } T \geq 1873 \text{ K}, \end{cases} \quad (\text{A.4b})$$

$$c_p^{[\text{CIns}]}(T) = 2100 \frac{\text{J}}{\text{kg K}}, \quad (\text{A.4c})$$

$$\varepsilon^{[\text{CIns}]}(T) = 0.53 \quad (\text{A.4d})$$

where

$$\begin{aligned} a_{\kappa}^{[\text{CIns}]} &= -\frac{609396292308373774083543}{512} \cdot 10^{-19}, \\ b_{\kappa}^{[\text{CIns}]} &= \frac{355163131482778204191}{1024} \cdot 10^{-18}, \\ c_{\kappa}^{[\text{CIns}]} &= -\frac{204652204018369767}{512} \cdot 10^{-18}, \quad d_{\kappa}^{[\text{CIns}]} = \frac{116893623135279}{512} \cdot 10^{-18}, \\ e_{\kappa}^{[\text{CIns}]} &= -\frac{66155269623}{1024} \cdot 10^{-18}, \quad f_{\kappa}^{[\text{CIns}]} = \frac{37145151}{512} \cdot 10^{-19}. \end{aligned} \quad (\text{A.5})$$

$\rho^{[\text{CIns}]}$, $\kappa^{[\text{CIns}]}$ and $c_p^{[\text{CIns}]}$ are as provided by [MSS99] where $\kappa^{[\text{CIns}]}$ has been fitted according to Table 3. Since no data for the emissivity of graphite felt were available we used the value given for carbon filament in [Lid95, p. 10-297].

T [K]	673	873	1073	1273	1473	1673	1873	2073	2273
$\kappa \left[\frac{\text{W}}{\text{m K}} \right]$	0.25	0.3	0.35	0.39	0.45	0.5	0.67	0.82	0.95

Table 3: Thermal conductivity of graphite felt according to [MSS99].

A.2.3 SiC Source Powder

$$\rho^{[\text{SiCP}]}(T) = 1700 \frac{\text{kg}}{\text{m}^3}, \quad (\text{A.6a})$$

$$\kappa^{[\text{SiCP}]}(T) = 6.83991 \cdot 10^{-3} e^{\frac{1.07296 \cdot 10^{-3} T}{\text{K}}} \frac{\text{W}}{\text{m K}}, \quad (\text{A.6b})$$

$$c_p^{[\text{SiCP}]}(T) = 1000 \frac{\text{J}}{\text{kg K}}, \quad (\text{A.6c})$$

$$\varepsilon^{[\text{SiCP}]}(T) = 0.85. \quad (\text{A.6d})$$

(A.6a) and (A.6c) are according to [MSS99]. The data for the total emissivity $\varepsilon^{[\text{SiCP}]}$ provided by [TdW72, p. 793] vary between 0.3 and 0.9, most data lying between 0.8 and 0.9. Thus (A.6d) seems to be a reasonable assumption. [KRRS98] describes the dependence of the thermal conductivity of SiC powder on its porosity, its particle sizes, its transmissivity and the ambient gas pressure. The common features of the presented results are that the range of the thermal conductivity lies between $5 \cdot 10^{-3} \frac{\text{W}}{\text{m K}}$ and $5 \cdot 10^{-1} \frac{\text{W}}{\text{m K}}$ and that the thermal conductivity usually increases with temperature. In absence of precise data for the porosity and particle sizes of SiC powder used in actual growth experiments, we think it is justified to use the simple approximation given in (A.6b).

A.2.4 SiC Single Crystal

$$\rho^{[\text{SiCC}]}(T) = 3140 \frac{\text{kg}}{\text{m}^3}, \quad (\text{A.7a})$$

$$\kappa^{[\text{SiCC}]}(T) = \frac{61100}{\frac{T}{\text{K}} - 115} \frac{\text{W}}{\text{m K}}, \quad (\text{A.7b})$$

$$c_p^{[\text{SiCC}]}(T) = \frac{\frac{\text{J}}{\text{kg K}}}{39161 \left[\frac{T}{\text{K}}\right]^{-3.17377} + 1.83598 \cdot 10^{-3} \left[\frac{T}{\text{K}}\right]^{-0.117995}}, \quad (\text{A.7c})$$

$$\varepsilon^{[\text{SiCC}]}(T, \lambda) = 0.85 \quad \text{on} \quad I_r. \quad (\text{A.7d})$$

$\rho^{[\text{SiCC}]}$ and $\kappa^{[\text{SiCC}]}$ are according to [NMH⁺97]. $c_p^{[\text{SiCC}]}$ has been fitted according to [BK73, p. 1342]. In absence of other data we use the constant value from (A.6d) for the emissivity $\varepsilon^{[\text{SiCC}]}(T, \lambda)$ in the reflective band I_r . As mentioned in [BK90, p. 2833], the energy gap for the 6H polytype shifts from 3 eV (corresponding to $I_r = [0, 413 \text{ nm}]$) at 300 K to some 2.5 eV (corresponding to $I_r = [0, 495 \text{ nm}]$) at 2400 K, indicating that the energy-band model of semi-transparency is not completely accurate if the range of temperatures is large. In the simulations of Section 3.3 we assumed that the band of wavelengths interacting with the crystal is $I_r = [1 \text{ nm}, 500 \text{ nm}]$.

Acknowledgements

The *Institut für Kristallzüchtung* in Berlin has provided us with physical data throughout the project. We particularly wish to thank Dr. Dietmar Siche, Detlev Schulz and Thomas Müller for providing the experimentalists' feedback that is essential for our research.

Special thanks is due to Dr. Volker Weiß who provided most of the references for material data from the literature presented in Appendix A.

This research was partly funded by the *Bundesministerium für Bildung, Wissenschaft, Forschung und Technologie (BMBF)*, number 03SP7FV16 of the project *Mathematische Verfahren zur Lösung von Problemstellungen in Industrie und Wirtschaft*.

References

- [ABEP98] J. AUBRETON, E. BLANQUET, M.F. ELCHINGER, and M. PONS, *Les Différentes Voies de Modélisation Macroscopique du Procédé de Dépôt de SiC par Voie Gazeuse*, Ann. Chim. Sci. Mat. **23** (1998), 753–789.
- [BK73] I. BARIN and O. KNACKE, *Thermodynamical Properties of Inorganic Substances*, Springer, 1973.
- [BK90] D.P. BIRNIE and W.D. KINGERY, *The limit of non-stoichiometry in silicon carbide*, Journal of Materials Science **25** (1990), 2827–2834.
- [BKP⁺99] N. BUBNER, O. KLEIN, P. PHILIP, J. SPREKELS, and K. WILMAŃSKI, *A transient model for the sublimation growth of silicon carbide single crystals*, Journal of Crystal Growth **205** (1999), 294–304.
- [BMH⁺93] D.L. BARRET, J.P. MCHUGH, H.M. HOBGOOD, R.H. HOPKINS, P.G. McMULLIN, R.C. CLARKE, and W.J. CHOYKE, *Growth of large SiC single crystals*, Journal of Crystal Growth **128** (1993), 358–362.
- [CC70] S. CHAPMAN and T.G. COWLING, *The mathematical theory of non-uniform gases*, Cambridge University Press, Cambridge, Great Britain, 1970.
- [DNR⁺90] F. DUPRET, P. NICODÉME, Y. RYCKMANS, P. WOUTERS, and M.J. CROCHET, *Global modelling of heat transfer in crystal growth furnaces*, Int. J. Heat Mass Transfer **33** (1990), no. 9, 1849–1871.
- [FKL98] J. FUHRMANN, TH. KOPRUCKI, and H. LANGMACH, *pdelib: An open modular tool box for the numerical solution of partial differential equations. Design patterns*, Proceedings of the 14th GAMM Seminar on Concepts of Numerical Software, Kiel, Notes on Numerical Fluid Mechanics, Vieweg, Braunschweig, 1998, to press.

- [Fuh97] J. FUHRMANN, *On numerical solution methods for nonlinear parabolic problems*, Modeling and Computation in Environmental Sciences, Notes on Numerical Fluid Mechanics, vol. 59, Vieweg, Braunschweig/Wiesbaden, 1997, pp. 170–180.
- [Har95] G. L. HARRIS (ed.), *Properties of Silicon Carbide*, Institution of Electrical Engineers, INSPEC, London, 1995.
- [HHW⁺95] D. HOFMANN, M. HEINZE, A. WINNACKER, F. DURST, L. KADINSKI, P. KAUFMANN, Y. MAKAROV, and M. SCHÄFER, *On the sublimation growth of SiC bulk crystals: development of a numerical process model*, Journal of Crystal Growth **146** (1995), 214–219.
- [Jär96] J. JÄRVINEN, *Mathematical Modeling and Numerical Simulation of Czochralski Silicon Crystal Growth*, Ph.D. thesis, University of Jyväskylä, 1996.
- [Kan93] T. KANEKO, *Growth kinetics of vapour-grown SiC*, Journal of Crystal Growth **128** (1993), 354–357.
- [Kon95] A.O. KONSTANTINOV, *Sublimation growth of SiC*, In Harris [Har95], pp. 170–203.
- [KRRS98] E.L. KITANIN, M.S. RAMM, V.V. RIS, and A.A. SCHMIDT, *Heat transfer through source powder in sublimation growth of SiC crystal*, Materials Science and Engineering B **55** (1998), 174–183.
- [Lid95] D.R. LIDE (ed.), *CRC Handbook of Chemistry and Physics*, CRC Press, Boca Raton, 1995.
- [Lil93] S.K. LILOV, *Study of the equilibrium processes in the gas phase during silicon carbide sublimation*, Material Science and Engineering **B21** (1993), 65–69.
- [MSS99] T. MÜLLER, D. SCHULZ, and D. SICHE, Institut für Kristallzüchtung, Berlin, 1999, Private communication.
- [Nis95] S. NISHINO, *Bulk growth of SiC*, In Harris [Har95], pp. 163–169.
- [NMH⁺97] O. NILSSON, H. MEHLING, R. HORN, J. FRICKE, R. HOFMANN, S.G. MÜLLER, R. ECKSTEIN, and D. HOFMANN, *Determination of the thermal diffusivity and conductivity of monocrystalline silicon carbide (300–2300 K)*, High Temperatures - High Pressures **29** (1997), no. 1, 73–80.
- [PBD⁺96] M. PONS, E. BLANQUET, J.M. DEDULLE, I. GARCON, R. MADAR, and C. BERNARD, *Thermodynamic heat transfer and mass transport modelling of the sublimation growth of silicon carbide crystals*, J. Electrochem. Soc. (1996).

- [TdW72] Y.S. TOULOUKIAN and D.P. DE WITT (eds.), *Thermal radiative properties - nonmetallic solids*, Thermophysical Properties of Matter: The TPRC Data Series, vol. 8, IFI/Plenum, New York, 1972.
- [Var75] N.B. VARGAFTIK, *Tables on the Thermophysical Properties of Liquids and Gases*, Hemisphere, Washington, D.C., 1975.